Gravity Waves Generated by Sheared Three-Dimensional Potential Vorticity Anomalies

FRANÇOIS LOTT AND RIWAL PLOUGONVEN

Laboratoire de Météorologie Dynamique du CNRS, Ecole Normale Supérieure, Paris, France

JACQUES VANNESTE

School of Mathematics and Maxwell Institute for Mathematical Sciences, University of Edinburgh, Edinburgh, United Kingdom

(Manuscript received 31 October 2011, in final form 28 February 2012)

ABSTRACT

The gravity waves (GWs) produced by three-dimensional potential vorticity (PV) anomalies are examined under the assumption of constant vertical shear, constant stratification, and unbounded domain. As in the two-dimensional case analyzed in an earlier paper, the disturbance near the PV anomaly is well modeled by quasi-geostrophic theory. At larger distances the nature of the disturbance changes across the two inertial layers that are located above and below the anomaly, and it takes the form of a vertically propagating GW beyond these.

For a horizontally monochromatic PV anomaly of infinitesimal depth, the disturbance is described analytically using both an exact solution and a WKB approximation; the latter includes an exponentially small term that captures the change of the solution near the PV anomaly induced by the radiation boundary condition in the far field. The analytical results reveal a strong sensitivity of the emission to the Richardson number and to the orientation of the horizontal wavenumber: the absorptive properties of the inertial layers are such that the emission is maximized in the Northern Hemisphere for wavenumbers at negative angles to the shear.

For localized PV anomalies, numerical computations give the temporal evolution of the GW field. Analytical and numerical results are also used to establish an explicit form for the Eliassen–Palm flux that could be used to parameterize GW sources in GCMs. The properties of the Eliassen–Palm flux vector imply that in a westerly shear, the GWs exert a drag in a southwest direction in the upper inertial layer, and in a northwest direction at the altitudes where the GWs dissipate aloft.

1. Introduction

Spontaneous adjustment, the mechanism whereby a well-balanced flow radiates gravity waves (GWs) in the course of its near-balanced evolution (Ford et al. 2000; Vanneste and Yavneh 2004; Vanneste 2008), is a possible source of atmospheric GWs. It can be distinguished from other mechanisms, including topographic forcing and the classical adjustment originally described in Rossby (1937), by the fact that it involves no process external to the flow itself. In realistic configurations, however, spontaneous adjustment is mixed with other mechanisms. For instance, large mountain GWs produce potential vorticity (PV) anomalies when they break (Schär and Smith 1993), as well as secondary GWs (Scavuzzo et al. 1998). To measure the relative importance of these two signals, Lott (2003) studied the large-scale response to mountain-wave breaking near critical levels and showed that substantial GWs are reemitted during the breaking itself, while the long-term evolution is dominated by the balanced response. Martin (2008) subsequently found that the PV field associated with the balanced response radiates GWs well after the end of the initial breaking. This emission, although weaker than the initial one, is potentially more persistent since it is tied to the slowly evolving PV. It is plausible, therefore, that it contributes to the low-frequency GWs observed in the wakes of breaking topographic waves (Plougonven et al. 2010).

Corresponding author address: François Lott, Laboratoire de Météorologie Dynamique du CNRS, Ecole Normale Supérieure, 24, rue Lhomond, 75231 Paris CEDEX 05, France.
E-mail: flott@lmd.ens.fr

DOI: 10.1175/JAS-D-11-0296.1

To quantify this emission by PV more precisely, Lott et al. (2010, hereafter LPV10) examined the GWs emitted by small-amplitude PV anomalies in a shear. In this scenario, the separation between balanced motion and GWs does not hold: because of the Doppler shift, motions that are balanced in the vicinity of the anomalies become, in the far field, gravity waves [see also Plougonven et al. (2005); Mamatsashvili et al. (2010)]. In the linear approximation, and assuming constant wind shear Λ and constant Brunt–Väisälä frequency N, LPV10 found that substantial GWs reach the far field when the Richardson number $J = N^2/\Lambda^2$ is not too large (say, between 1 and 10). By substantial, we mean that, for PV anomalies representative of those likely to be found when thin layers of stratospheric air enter the troposphere, the Eliassen–Palm (EP; or pseudomomentum) flux associated with the GWs is comparable to that measured in the stratosphere far from mountains (Hertzog et al. 2008).

A practical result of LPV10 is a simple analytical estimate for the EP flux that could be used in general circulation models (GCMs) that include the stratosphere. In nondimensional form, this estimate is given by

$$\mathcal{F} \sim \frac{1}{4} e^{-\pi\sqrt{J}}. \tag{1.1}$$

LPV10 also showed that half of this flux is absorbed in the inertial layers above and below the PV anomaly while the other half is radiated in the far field as GWs. The dimensional EP flux follows from (1.1) by multiplication by the scaling factor

$$F_0 = \frac{\rho_r g^2}{f\theta_r^2 N^3}(\rho_r q_r \sigma_z)^2, \tag{1.2}$$

where g is the gravity constant, f the Coriolis parameter, ρ_r and θ_r background reference values for the density and potential temperature, q_r the amplitude of the PV anomaly, and σ_z its depth. In a GCM, these last two quantities could be related to the grid-scale PV value and to the vertical grid spacing.

A limitation of LPV10 is the restriction to two-dimensional PV anomalies, with no structure in the direction transverse to the basic shear. This is a significant limitation since the absorption of GWs at inertial levels strongly depends on the orientation of the horizontal wave vector. This is known from the investigations on GW propagating upward toward inertial levels: Grimshaw (1975) and Yamanaka and Tanaka (1984) showed that the absorption at the lowest inertial level is large for $\nu\Lambda < 0$, where $\nu = l/k$ is the ratio between the transverse and parallel horizontal wavenumbers, and much smaller for $\nu\Lambda > 0$. This results in a "valve effect," which Yamanaka (1985) interpreted by analyzing the tilt of the phase lines of the GWs (i.e., of particle displacements) relative to the isentropes. The configuration that we analyze is quite different since the GW associated with a PV disturbance is generated between the critical levels and propagates outwards of them. Nevertheless, the argument of Yamanaka (1985) applies and we find strong absorption at the inertial level if $\nu\Lambda > 0$ and much weaker absorption if $\nu\Lambda < 0$.

The motivation of the present paper is to extend the results in LPV10 to three-dimensional PV anomalies. Accordingly, its first aim is to obtain the vertical structure of the 3D singular modes associated with PV anomalies that have the form of a Dirac function in the vertical. The analytic results derived for monochromatic anomalies can then be integrated to obtain the vertical structure associated with anomalies of arbitrary horizontal structure and show, in particular, that a horizontally isotropic PV anomaly produces a very specific anisotropic GW signature beyond the inertial levels. A second aim is to deduce further, by integration over the continuous spectrum, the GW response to a vertically smooth, localized PV distribution. A third aim is to extend the EP flux predictions in (1.1) and (1.2) to the 3D case. In this case, the (vertical component of the) EP flux, which can also be interpreted as a wave stress, is a horizontal vector. For a horizontally isotropic shear in the Northern Hemisphere, this vector is shown to make an angle with the shear that decreases with altitude, from zero at the anomaly level to some negative value in the far field. This implies that a PV anomaly in a westerly shear exerts a drag that is oriented to the southwest in the upper inertial region and to the northwest where the associated GW dissipates aloft.

The plan of the paper is as follows. The general formulation of the problem and its transformation to a dimensionless form are given in section 2. There we discuss both the exact response to a δ-PV distribution in the vertical, and its Wentzel–Kramers–Brillouin (WKB) approximation valid for $J \gg 1$. The WKB analysis extends that of LPV10 by resolving the Stokes phenomenon associated with the existence of an exponentially small (in J) contribution to the solution that grows exponentially between the PV anomaly and the inertial levels. Taking this contribution into account, we obtain a 3D generalization of the EP flux estimate (1.1). Section 3 presents the vertical structure of the response in some detail. It emphasizes the directional aspects and relates them to the tilt of the solution about isentropes in the meridional plane. Section 4 recasts the results in dimensional form and considers PV distributions that are

localized horizontally and that have a finite depth, in which case the GW response is transient. Section 5 summarizes the results. Appendixes A and B provide technical details on the exact and WKB solutions, respectively.

2. Formulation

a. Disturbance equations and potential vorticity

In the absence of mechanical and diabatic forcings, the linearized hydrostatic–Boussinesq equations for a three-dimensional disturbance in the shear flow $\overline{\mathbf{u}}_0 = (\Lambda z, 0, 0)$ read

$$(\partial_t + \Lambda z \partial_x)u' + \Lambda w' - fv' = -\frac{1}{\rho_r}\partial_x p', \quad (2.1a)$$

$$(\partial_t + \Lambda z \partial_x)v' + fu' = -\frac{1}{\rho_r}\partial_y p', \quad (2.1b)$$

$$0 = -\frac{1}{\rho_r}\partial_z p' + g\frac{\theta'}{\theta_r}, \quad (2.1c)$$

$$(\partial_t + \Lambda z \partial_x)g\frac{\theta'}{\theta_r} - f\Lambda v' + N^2 w' = 0, \quad \text{and} \quad (2.1d)$$

$$\partial_x u' + \partial_y v' + \partial_z w' = 0. \quad (2.1e)$$

Here u', v', and w' are the three components of the velocity disturbance, p' is the pressure disturbance, θ' is the potential temperature disturbance, and $N^2 = g\overline{\theta}_{0z}/\theta_r$ is the square of the constant Brunt–Väisälä frequency, with $\overline{\theta}_0(y, z)$ being the background potential temperature. Without loss of generality we assume that $\Lambda > 0$.

Equations (2.1a)–(2.1e) imply the conservation equation

$$(\partial_t + \Lambda z \partial_x)q' = 0, \quad (2.2)$$

for the PV perturbation

$$q' = \frac{1}{\rho_r}[\overline{\theta}_{0z}(\partial_x v' - \partial_y u') + \overline{\theta}_{0y}\partial_z u' + \Lambda\theta'_y + f\partial_z\theta']. \quad (2.3)$$

It follows that the PV at any time t is given explicitly in terms of the initial condition $q'_0(x, y, z) = q'(x, y, z, t = 0)$ by

$$q'(x, y, z, t) = q'_0(x - \Lambda z t, y, z). \quad (2.4)$$

b. Normal-mode decomposition

To evaluate the disturbance field associated with the PV anomaly (2.4), we express this solution in Fourier space,

$$q'(x, y, z, t) = \iint \hat{q}(k, l, z, t)e^{ikx+ily}\,dk\,dl = \iint \hat{q}_0(k, l, z)e^{i(kx+ly-k\Lambda zt)}\,dk\,dl, \quad (2.5)$$

where $\hat{q}_0$ is the horizontal Fourier transform of q'_0:

$$\hat{q}_0(k, l, z) = \frac{1}{4\pi^2}\int_{-\infty}^{\infty}\int_{-\infty}^{\infty} q'_0(x, y, z)e^{-i(kx+ly)}\,dx\,dy. \quad (2.6)$$

Here and henceforth integrations without limits are understood to be over the whole space. We rewrite (2.5) in the form

$$q'(x, y, z, t) = \frac{k\Lambda}{f}\iiint \hat{q}_0(k, l, z')e^{i(kx+ly-k\Lambda z't)}\delta\left[\frac{k\Lambda}{f}(z - z')\right]dz'\,dk\,dl, \quad (2.7)$$

where $\delta(\xi)$ is the Dirac function of the variable

$$\xi = \frac{k\Lambda}{f}(z - z'). \quad (2.8)$$

Note that (2.7) can be interpreted as the expansion of the perturbation PV in the (singular) normal modes of (2.3); these modes form a continuum, parameterized by the phase speed $\Lambda z'$. The scaling used in (2.8) places the inertial levels $z = z' \pm f/(k\Lambda)$ of these modes at $\xi = \pm 1$ (Inverarity and Shutts 2000).

The expansion of the vertical velocity w' corresponding to the expansion (2.7) of the PV can be written as

$$w'(x, y, z, t) = \iiint \hat{w}_0(k, l, z')e^{i(kx+ly-k\Lambda z't)}W\left[\frac{k\Lambda}{f}(z - z')\right]dz'\,dk\,dl, \quad (2.9)$$

where $\hat{w}_0(k, l, z')$ is the amplitude of the normal mode and $W(\xi)$ is its vertical structure. Note that this expansion describes the part of w' slaved to the PV: an additional continuum of singular modes, representing free sheared

GWs, would need to be added to the expansion to solve an arbitrary initial-value problem.

The velocities u' and v' and the potential temperature θ' have expansions analogous to (2.9), with $\hat{w}_0$ replaced by $\hat{u}_0$, $\hat{v}_0$, and $\hat{\theta}_0$, and W replaced by U, V, and Θ, respectively. Introducing these expansions into (2.1a)–(2.1e) and choosing

$$\hat{u}_0 = i\frac{\Lambda}{f}\hat{w}_0, \quad \hat{v}_0 = -\frac{\Lambda}{f}\hat{w}_0, \quad \text{and} \quad \hat{\theta}_0 = i\frac{\theta_r\Lambda^2}{fg}\hat{w}_0 \tag{2.10}$$

gives

$$U = \frac{\xi - i\nu}{\xi(1+\nu^2)}W_\xi + \frac{\nu^2}{\xi(1+\nu^2)}W,$$
$$V = \frac{1 - i\nu\xi}{\xi(1+\nu^2)}W_\xi + \frac{i\nu}{\xi(1+\nu^2)}W, \quad \text{and} \tag{2.11a}$$
$$\Theta = \frac{1 - i\nu\xi}{\xi^2(1+\nu^2)}W_\xi + \left[\frac{i\nu}{\xi^2(1+\nu^2)} + \frac{J}{\xi}\right]W, \tag{2.11b}$$

where $\nu = l/k$. We now introduce (2.10)–(2.11), into the expressions (2.3) and (2.7) for the PV. Choosing the vertical-velocity amplitude

$$\hat{w}_0(k,l,z') = -i\frac{\rho_r g(1+\nu^2)}{\theta_r\Lambda^2}\hat{q}_0(k,l,z') \tag{2.12}$$

then leads to the differential equation

$$\left(\frac{1-\xi^2}{\xi^2}\right)W_{\xi\xi} - \left(\frac{2}{\xi^3} - \frac{2i\nu}{\xi^2}\right)W_\xi - \left[\frac{(1+\nu^2)J}{\xi^2} + \frac{2i\nu}{\xi^3}\right]W = \delta(\xi), \tag{2.13}$$

for the structure function $W(\xi)$. Note that W depends on J and ν in addition to ξ, and that we use the notation $W(\xi)$ as a shorthand for the more complete but more cumbersome $W(J, \nu; \xi)$.

In appendix A, we follow Yamanaka and Tanaka (1984), Plougonven et al. (2005), and LPV10 and solve this equation exactly using a change of variable that transforms the homogeneous part of (2.13) into the hypergeometric equation. The solution satisfies

$$W(\xi) \sim E\xi^{1/2+i\sqrt{J(1+\nu^2)-1/4}} \quad \text{as} \quad \xi \to +\infty, \quad \text{and} \tag{2.14}$$

$$W(\xi) = W^*(-\xi) \quad \text{for} \quad \xi < 0, \tag{2.15}$$

corresponding to an upward (downward)-propagating GW as $\xi \to +\infty$ ($\xi \to -\infty$). An explicit expression for the amplitude E of this GW is given in (A.13).

c. WKB approximation

In the limit $J \gg 1$, it is possible to derive an approximation to $W(\xi)$ using a WKB approach. This approximation, which we now derive, is more transparent than the exact solution in terms of hypergeometric functions and proves remarkably accurate for moderately large J.

We focus on the region $\xi > 0$ since the solution for $\xi < 0$ follows immediately from (2.15). The WKB approximation does not provide a single solution that is valid uniformly in $\xi > 0$; instead, four regions, which we label (i)–(iv), need to be distinguished. The form of the solution in each of these regions, given below, is derived in appendix B.

In region (i), close to the PV anomaly and specifically for $\xi = O(J^{-1/2}) \ll 1$, the quasigeostrophic (QG) approximation applies, leading to

$$W^{(\mathrm{i})}(\xi) \sim A^{(\mathrm{i})}\left[\sqrt{J(1+\nu^2)}\xi + 1\right]e^{-\sqrt{J(1+\nu^2)}\xi} + B^{(\mathrm{i})}\left[\sqrt{J(1+\nu^2)}\xi - 1\right]e^{\sqrt{J(1+\nu^2)}\xi}. \tag{2.16}$$

One solution is exponentially decaying away from the PV anomaly, consistent with the expectation from the QG approximation. The other, an exponentially growing solution, is absent in the standard QG approximation but will need to be retained in order to derive the EP flux between the inertial levels, as discussed below.

In region (ii), between the PV anomaly and the inertial level, and more precisely where $\xi = O(1)$ and $\xi < 1$,

$$W^{(\mathrm{ii})}(\xi) \sim \frac{\xi}{(1-\xi)^{1/4-i\nu/2}(1+\xi)^{1/4+i\nu/2}} \times \left[A^{(\mathrm{ii})}e^{-\sqrt{J(1+\nu^2)}\sin^{-1}\xi} + B^{(\mathrm{ii})}e^{\sqrt{J(1+\nu^2)}\sin^{-1}\xi}\right]. \tag{2.17}$$

In region (iii), close enough to the inertial level that $|\xi - 1| = O(J^{-1})$, the solution is expressed in terms of the scaled variable $\zeta = J(1+\nu^2)(\xi - 1)$ as

$$W^{(\mathrm{iii})}(\xi) \sim \zeta^{i\nu/2}\left[A^{(\mathrm{iii})}H^{(1)}_{i\nu}(\sqrt{2\zeta}) + B^{(\mathrm{iii})}H^{(2)}_{i\nu}(\sqrt{2\zeta})\right], \tag{2.18}$$

where $H^{(1)}_{i\nu}$ and $H^{(2)}_{i\nu}$ are Hankel functions (Abramowitz and Stegun 1964).

Finally, in region (iv) above the inertial level where $\xi = O(1)$ and $\xi > 1$, the solution is

$$W^{(\mathrm{iv})}(\xi) \sim \frac{\xi}{(\xi-1)^{1/4-i\nu/2}(\xi+1)^{1/4+i\nu/2}} \times \left[A^{(\mathrm{iv})}e^{i\sqrt{J(1+\nu^2)}\ln(\xi+\sqrt{\xi^2-1})} + B^{(\mathrm{iv})}e^{-i\sqrt{J(1+\nu^2)}\ln(\xi+\sqrt{\xi^2-1})}\right]. \tag{2.19}$$

The eight constants $A^{(i)}\cdots B^{(iv)}$ are fixed by imposing a jump conditions at $\xi = 0$ given in (A.1), a radiation condition as $\xi \to \infty$, and continuity of the solution across the four regions. Starting with the radiation condition, we obtain from (2.14) and (2.19) that

$$A^{(iv)} = 2^{i\sqrt{J(1+\nu^2)}}E \quad \text{and} \quad B^{(iv)} = 0. \tag{2.20}$$

Matching between regions (iv) and (iii) then gives

$$A^{(iv)} = 2^{1/2+i\nu/2}\pi^{-1/2}[J(1+\nu^2)]^{-1/4+i\nu/2}e^{\nu\pi/2}e^{-i\pi/4}A^{(iii)} \quad \text{and} \quad B^{(iii)} = 0 \tag{2.21}$$

(see appendix B for details).

Some care needs to be exercised when matching from region (iii) to region (ii). Standard matching as carried out in LPV10 gives $B^{(ii)} = 0$, in agreement with the expectation from quasigeostrophic theory of a solution that decays exponentially with altitude above $\xi = 0$. This solution is not entirely satisfactory, however, in that it fails to capture the feedback that radiation (as $\xi \to \infty$) has on the solution in regions (ii) and (i). In particular, a single exponentially decaying solution [in regions (i) and (ii)] has a zero EP flux, inconsistent with the nonzero flux from the exact solution. To resolve this apparent difficulty, we need to recognize that $B^{(ii)} = 0$ is only an approximation. In fact, $B^{(ii)}$ takes an exponentially small, nonzero value, which can be captured using the more sophisticated matching procedure applied in appendix B. This procedure yields

$$A^{(iii)} = 2^{-1/2-i\nu/2}\pi^{1/2}[J(1+\nu^2)]^{1/4-i\nu/2}e^{-\pi/2\sqrt{J(1+\nu^2)}-\nu\pi}A^{(ii)}, \tag{2.22}$$

$$B^{(ii)} = -ie^{-\sqrt{J(1+\nu^2)}\pi}\cosh(\nu\pi)A^{(ii)}. \tag{2.23}$$

Equation (2.23) implies that the exponentially decaying solution of quasigeostrophic theory in regions (i) and (ii) is always accompanied by an exponentially growing solution. The amplitude of this solution is exponentially small in region (ii) but becomes comparable to the decaying solution as $\xi \to 1$. This combination of exponentially growing and decaying solutions is enforced by the radiation condition and is consistent with the consequent nonzero EP flux. By retaining the exponentially small $B^{(ii)}$ [in spite of the neglect of much larger $O(J^{-1/2})$ terms in the dominant solution], we capture this important part of the physics of the problem. A comparable situation arises for the Schrödinger equation in quantum mechanics, in the semiclassical study of wave propagation through a potential barrier (e.g., Bender and Orszag 1999). In this context, a wavelike solution radiating outside the barrier is associated with a combination of exponentially decaying and exponentially growing solutions inside the barrier. While the solution that decays toward the interior of the barrier (and corresponds to $B^{(ii)}$ in our problem) is usually neglected (Bender and Orszag 1999), it can be retained (e.g., to obtain a direct estimate of the so-called decay width; Shepard 1983).

The WKB solution is completed by matching regions (i) and (ii) to obtain

$$A^{(ii)} = \sqrt{J(1+\nu^2)}A^{(i)} \quad \text{and} \quad B^{(ii)} = \sqrt{J(1+\nu^2)}B^{(i)}. \tag{2.24}$$

Taking (2.15) into account and applying the jump conditions (A.1) at $\xi = 0$ yields

$$A^{(i)} = \frac{1}{2[J(1+\nu^2)]^{3/2}}, \tag{2.25}$$

when neglecting an exponentially small term against $O(1)$ terms. It then follows that

$$B^{(i)} = -\frac{i}{2[J(1+\nu^2)]^{3/2}}e^{-\sqrt{J(1+\nu^2)}\pi}\cosh(\nu\pi), \tag{2.26}$$

which provides the amplitude of the exponentially growing solution in the quasigeostrophic region.

The amplitude of the GW radiating at $\xi \to \pm\infty$ will be found by combining (2.20), (2.21), (2.22), and (2.25). It is given by

$$|E| \sim \frac{e^{-\nu\pi/2}}{2J(1+\nu^2)}e^{-\pi\sqrt{J(1+\nu^2)}/2}. \tag{2.27}$$

This large-J approximation will be compared with the exact solution in section 3 and found to provide a reasonable estimate for J as small as 1.

d. EP flux

An important property of (2.13) is the conservation of the EP flux (Eliassen and Palm 1961), or pseudomomentum flux. Multiplying (2.13) by $J^{3/2}(1+\nu^2)W^*$ and integrating by parts results in a conservation for the nondimensional EP flux,

$$\mathcal{F} = \frac{J^{3/2}(1+\nu^2)^{3/2}}{2}\mathrm{Re}\left(i\frac{1-\xi^2}{\xi^2}W_\xi W^* - \nu\frac{WW^*}{\xi^2}\right) = \text{const}, \tag{2.28}$$

that is valid away from $\xi = 0, \pm 1$. The scaling factor on the left of the real part symbol is introduced so that $\mathcal{F}$ coincides with the conventional definition

$$\rho_r\left(-\overline{u'w'} + f\frac{\overline{v'\theta'}}{\theta_{0z}}\right) \tag{2.29}$$

of the EP flux (e.g., Andrews et al. 1987) up to the J-independent dimensional factor (1.2).

Using the fact that $W \sim E\xi^{1/2+i\sqrt{J(1+\nu^2)-1/4}}$ for $\xi \to \infty$ and the asymptotics in (A.14a) and (A.14b) for $\xi \ll 1$ gives

$$\mathcal{F} = \frac{J^{3/2}(1+\nu^2)^{3/2}}{2}\begin{cases} 3i(BA^* - B^*A)|E|^2/2 & \text{for} \quad |\xi| < 1, \\ \sqrt{J(1+\nu^2) - 1/4}|E|^2 & \text{for} \quad |\xi| > 1, \end{cases} \tag{2.30}$$

where A, B, and E are given explicitly in terms of Γ functions in appendix A. A more convenient expression is obtained by using the WKB form of W. To compute $\mathcal{F}$ below the inertial level, we introduce (2.16), (2.25), and (2.26) into (2.28); to compute $\mathcal{F}$ above the inertial level we introduce (2.27) into (2.30). The result is the large-J approximation

$$\mathcal{F} \sim e^{-\pi\sqrt{J(1+\nu^2)}}\begin{cases} \cosh(\nu\pi)/4 & \text{for} \quad |\xi| < 1, \\ e^{-\nu\pi}/8 & \text{for} \quad |\xi| > 1. \end{cases} \tag{2.31}$$

Note that the expression for $|\xi| < 1$ relies on our estimate (2.26) of the exponentially small constant $B^{(i)}$.

Equation (2.31) shows that inertial-level absorption results in a jump in the EP flux such that

$$\frac{\mathcal{F}(1^+)}{\mathcal{F}(1^-)} \sim \frac{1}{1 + e^{2\nu\pi}}. \tag{2.32}$$

This formula extends LPV10's result, which showed that for $\nu = 0$ half of the EP flux is deposited at the inertial level.

3. Results for $W(\xi)$

In this section we examine the structure of $W(\xi)$ and compare the exact solution with the WKB approximation.

a. Vertical structure

The four panels in Fig. 1 show $W(\xi)$ for $J = 4$ and for four different orientations of the horizontal wave vector $\mathbf{k} = (k, l) = K(\cos\varphi, \sin\varphi)$, with $\varphi = -45°, -15°, -15°, 45°$, that is for $\nu = -1, -0.267\ldots, 0.267\ldots, 1$ and $J = 4$. In all cases, the real part of W is approximated by its geostrophic estimate $W^{(i)}$ in (2.16) some distance away from the neighborhood of $\xi = 0$ where it is strictly valid. The imaginary part of W is substantially smaller than the real part, in particular near and around $\xi \approx 0$ where the quasigeostrophic approximation predicts a purely real $W^{(i)}$. The real and imaginary parts of W only become comparable near the inertial levels, where balanced approximations do not apply.

Between (and away from) the inertial levels $\xi = \pm 1$, Im(W) follows in quadrature Re(W) when $\nu < 0$, but precedes Re(W) in quadrature when $\nu > 0$. As discussed in the next subsection, this behavior implies that the solutions always tilt along the isentropes in the (y, z) plane. Note that this behavior is well captured by the WKB solution in (2.17) but that can also be captured by correcting the QG solution to higher order as in Plougonven et al. (2005). Beyond $\xi = \pm 1$ the solution almost behaves as a pure gravity wave solution, in agreement with the asymptotic approximation in (2.14). The real part of the latter is shown by the gray dots in Fig. 1.

The most striking feature in Fig. 1 is the strong sensitivity of W to ν. According to the WKB estimates, ν affects the amplitude of W in three ways. First near $\xi = 0$, W, decreases with increasing $|\nu|$, according to the approximation $W(0) = W^{(i)}(0) \sim [J(1 + \nu^2)]^{-3/2}/2$ obtained from (2.16) and (2.25). Second, the decay rate of W in region (ii), is given by $\sqrt{J(1 + \nu^2)}$ [see (2.17)] and thus increases with $|\nu|$. Third, the amplitude of W in the GW region (iv) depends strongly on ν through the factor $e^{-\nu\pi/2}$ in (2.27). The first two effects explain the decrease in W between $\xi = \pm 1$ from Figs. 1a,d to Figs. 1b,c. The third effect depends on the sign of ν; this introduces a meridional asymmetry and explains the changes from Fig. 1a to Fig. 1d and from Fig. 1b to Fig. 1c. We discuss this effect further in the next section.

b. Meridional asymmetry and valve effect

A strong meridional asymmetry in absorption was highlighted by Grimshaw (1975) and Yamanaka and Tanaka (1984) in their studies of GWs propagating upward toward a critical level surrounded by two inertial levels. The latter authors showed that there is a very strong absorption at the lowest inertial level if $\nu\Lambda < 0$. If $\nu\Lambda > 0$, the wave crosses the first inertial level with little attenuation, but it is almost entirely reflected downward at a turning point located between the critical level in $\xi = 0$ and the lowest inertial level in $\xi = -1$. The reflected wave is then strongly absorbed as it returns to the lowest inertial level. Even though in both scenarios the initial upward GW is ultimately absorbed at the lowest inertial level, this potential intrusion of the GW signal between the inertial levels is quite remarkable and was referred to as a ''valve'' effect by these authors. This effect was interpreted heuristically by Yamanaka (1985), who analyzed with detail the behavior of two independent solutions near the lowest inertial level. He pointed out that the phase lines of one of the solutions change direction rapidly around the inertial level, and lie between the horizontal plane and the isentropes in a narrow region. Applying a static-stability method to analyze the stability of the air parcels displaced along phase

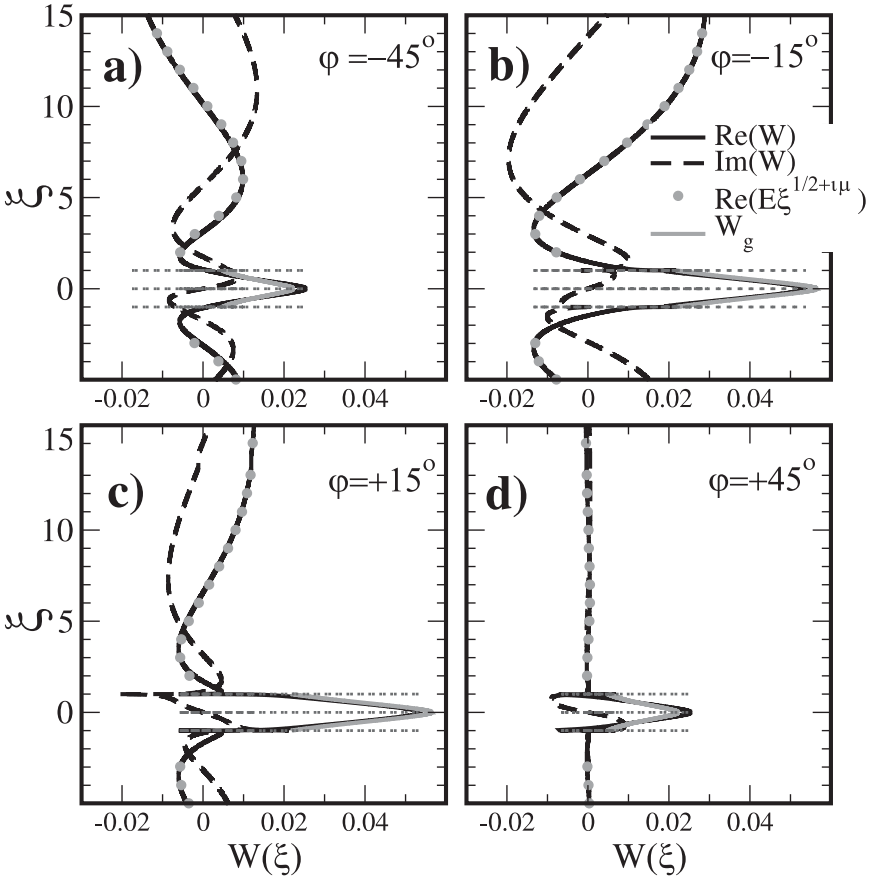

FIG. 1. Structure function $W(\xi)$ associated with a monochromatic PV distribution proportional to $\delta(\xi)$ for a Richardson number $J = 4$, and for different values of the wavenumber angle $\varphi = \tan^{-1}(\nu)$: (a) −45°, (b) −15°, (c) 15°, and (d) 45°. The thick black curves and thick dashed curves show the real and imaginary parts of $W(\xi)$, respectively. The gray dotted curves show the real part of the far-field gravity wave approximation $E\xi^{1/2+i\mu}$, and the thick gray curves show the quasigeostrophic approximation $W^{(i)}$. The location of $\xi = 0$ and of the inertia levels $\xi = \pm 1$ is also indicated.

lines leads to the conclusion that, for this solution, the region is baroclinically unstable (Pedlosky 1987).

A similar heuristic argument can be invoked to explain why the absorption at the inertial levels is much stronger for $\Lambda\nu > 0$ than $\Lambda\nu < 0$ (recall that we assume $\Lambda > 0$). If we follow Yamanaka and Tanaka (1984) and translate their description of the valve effect in our context, this sensitivity is related to the mathematical fact that around the inertial level in $\xi = 1$, the two independent solutions of (2.13),

$$W_1^{(1)} = (1+\xi)^{-i\nu} F(a, b; a + b + 1 - c; 1 - \xi^2) \quad \text{and} \tag{3.1a}$$

$$W_1^{(2)} = (\xi - 1)^{+i\nu} F(c - b, c - a; c - a - b + 1; 1 - \xi^2), \tag{3.1b}$$

behave very differently. The first changes smoothly through $\xi = 1$ whereas the second varies sharply and jumps by a multiplicative factor equal to $e^{\nu\pi}$ at $\xi = 1$ [see the analytical continuation in (A.8)].

Following Plougonven et al. (2005), a good way to assess the significance of these two solutions is to visualize them in the (y, z) plane (Figs. 2b,c,f,g). Figure 2b indicates that the smooth solution always tilts in the direction of the isentropes. In contrast, the other solution also tilts in the direction of the isentropes for $\xi < 1$ but tilts in the other direction for $\xi > 1$. The structure of the upward waves above $\xi = 1$, namely $\xi^{1/2+i\mu}e^{ily}$, also tilts in the direction of the isentropes when $\nu < 0$ but in the opposite direction when $\nu > 0$ (Figs. 2a,e). It is therefore not a surprise that the smooth solution plays the greater role to match the PV anomaly and the upward wave when $\nu < 0$, and that the other,

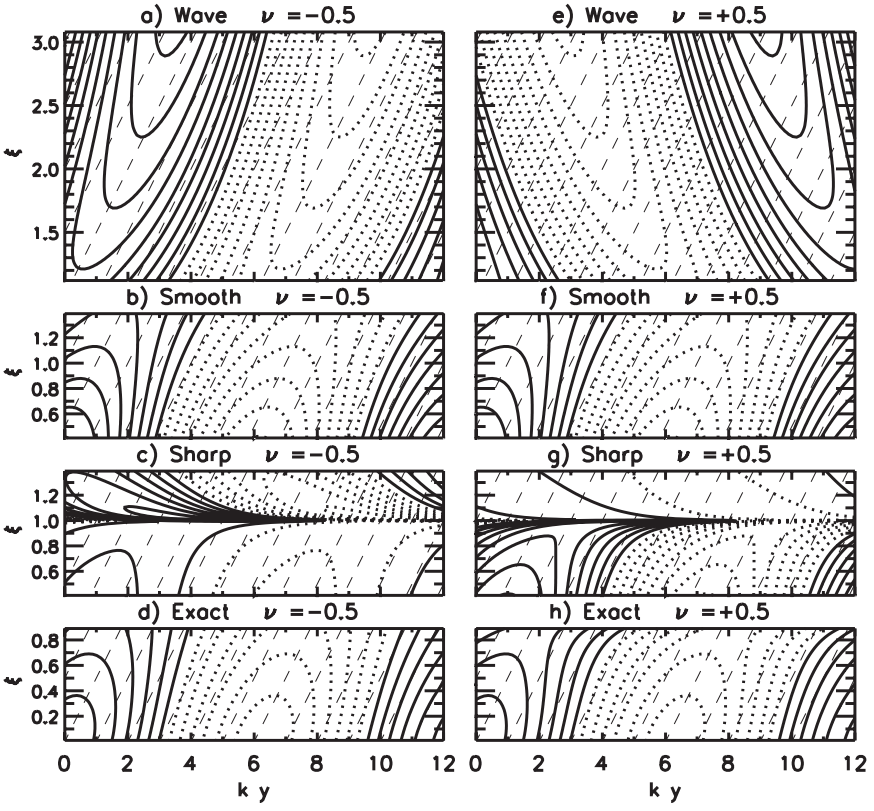

FIG. 2. Meridional structures of various solutions and approximations used to analyze $W(\xi)$ at the transition through the inertial level, for $J = 2$, and $\nu = \pm 0.5$: (a),(e): GW asymptotics $E\xi^{1/2+i\mu}e^{ily}$, (b),(f) smooth solution (3.1a) $W_1^{(1)}(\xi)e^{ily}$, (c),(g) sharp solution (3.1b) $W_1^{(2)}(\xi)e^{ily}$, and (d),(h) exact solutions (A.12). The contour intervals are arbitrary but are identical in (d) and (h). In all panels, the slope of the isentropes is indicated by the gray dashed lines.

rapidly changing solution plays the greater role when $\nu > 0$. Of course this can be checked analytically since the parameters α' and β' in (A.6b) exactly control the role of the rapidly changing and of the smooth solution in the connection through the upper critical level, respectively. It turns out that $|\alpha'/\beta'| = e^{\nu\pi}$, consistent with our argument.

Interestingly, the structures of the rapidly changing and smooth solutions are not much different well below $\xi = 1$ (e.g., cf. Figs. 2b and 2g between $\xi = 0.4$ and $\xi = 0.6$). In fact, the two solutions have the same Taylor expansion near $\xi = 0$ up to $O(\xi^3)$. According to (A.14a), this means that as $\xi \to 0$ both can equally be used to produce the δ-PV anomaly, which is consistent with the fact that the exact solutions around and above $\xi = 0$ are not much sensitive to the sign of ν (see Figs. 2d,h).

c. GW amplitude and EP flux

The combined effect of the two parameters J and ν on the GW emission is shown in Fig. 3, which compares the exact values of the GW amplitude $|E|$ with the WKB approximation (2.27). For a fixed value of ν, $|E|$ decreases with J as in LPV10. For fixed values of J, the cases with $\nu > 0$ and $\nu < 0$ need to be distinguished. For $\nu > 0$ and increasing, $|E|$ decreases monotonically as a result of increasing exponential decay in region (ii) and increasing inertial-level absorption. When $\nu < 0$ those two effects oppose: increasing $|\nu|$ increases the exponential decay but decreases the inertial-level absorption. Accordingly, $|E|$ is maximized for some $\nu(J) < 0$. Importantly, the WKB approximation (2.27) provides a good approximation for $|E|$ for $J \gtrsim 1$, well beyond the theoretical range of validity $J \gg 1$ of the asymptotics.

The EP flux within and outside the inertial levels are shown in Figs. 4a and 4b, respectively. The exact and WKB solutions (2.31) are compared. Figure 4a indicates that the EP flux between the inertial levels is only weakly sensitive to the angle $\varphi = \tan^{-1}\nu$ of the wave vector. It remains almost constant, for instance, for $-45° \lesssim \varphi \lesssim 45°$ when $J \approx 3$, or for $-30° \lesssim \varphi \lesssim +30°$ and $J \approx 10$. For larger values of φ, however, the EP flux decreases rapidly and vanishes for $\varphi = \pm\pi/2$. An important aspect of Fig. 4a is that the EP flux between the inertial levels is symmetric about the axis $\varphi = 0$.

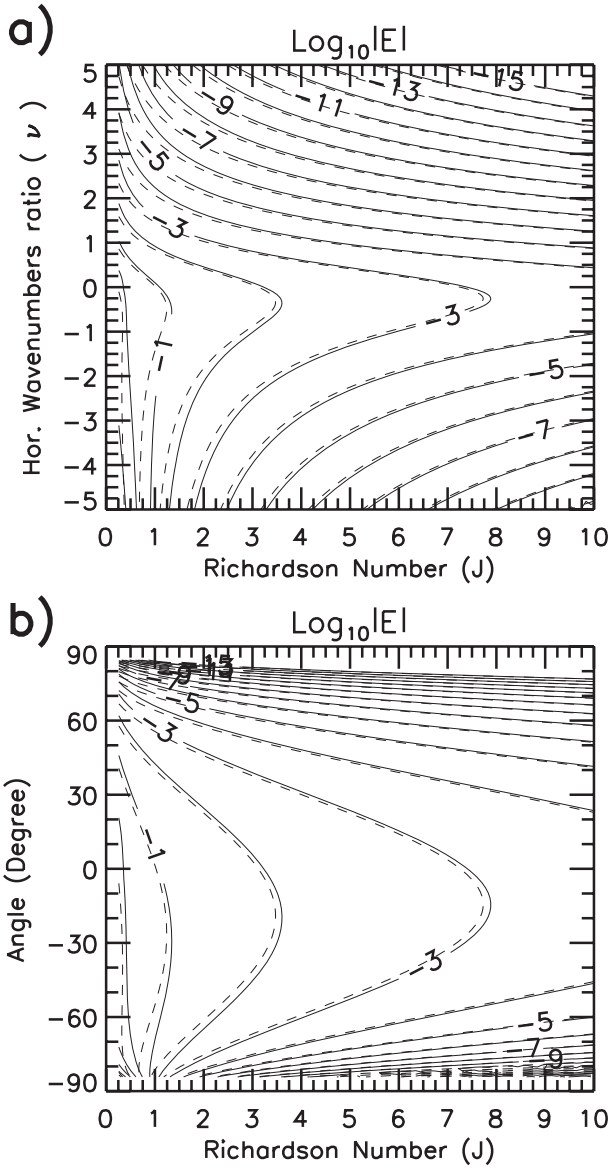

FIG. 3. Amplitude $|E|$ of the GW associated with a monochromatic Dirac PV anomaly as a function of J and (a) $\nu = l/k$ or (b) $\varphi = \tan^{-1}\nu$. The exact solution (solid) is compared with the WKB approximation (dashed).

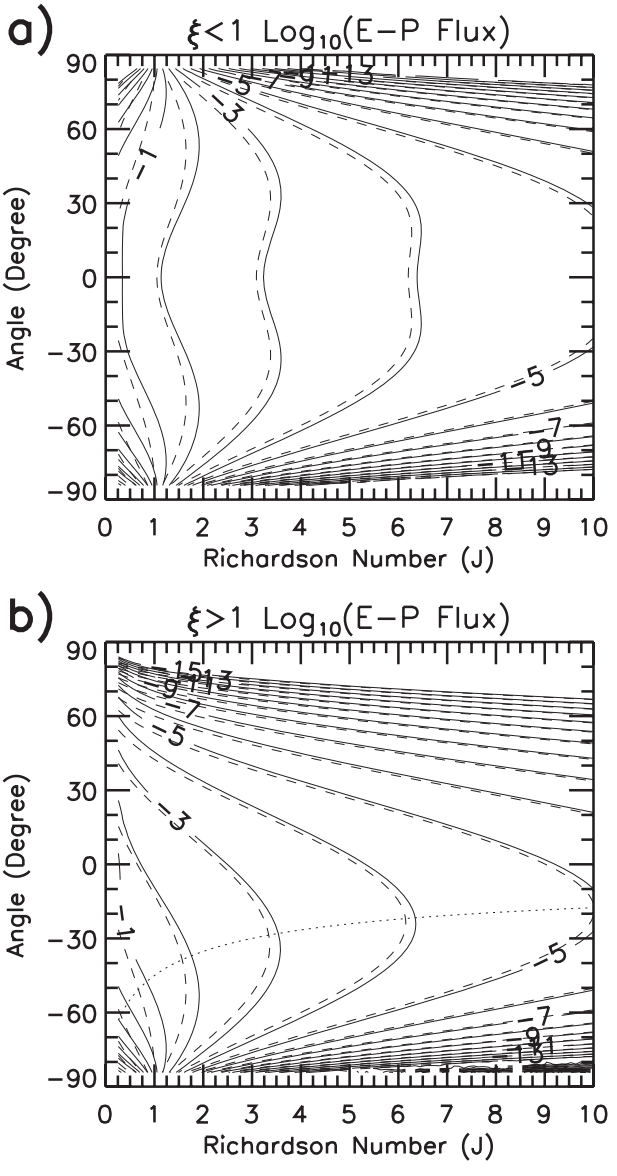

FIG. 4. EP flux associated with a monochromatic Dirac PV anomaly for (a) $|\xi| < 1$ and (b) $|\xi| > 1$. The exact solution (solid) is compared with the WKB approximation (dashed). The dotted line in (b) shows the WKB prediction of the angle maximizing $\mathcal{F}$.

This symmetry is broken outside the inertial levels (i.e., for $|\xi| > 1$) as a result of the asymmetric absorption at the inertial levels. This is clear from Fig. 4b: when $\varphi \lesssim -30°$ the EP fluxes for $|\xi| > 1$ are almost equal to the fluxes for $|\xi| < 1$, but they are much smaller for $\varphi \gtrsim 30°$. This is well captured by the WKB approximation (2.31), which again provides a good estimate for $J \gtrsim 1$ both for $|\xi| < 1$ and $|\xi| > 1$. In particular, it leads to the prediction

$$\nu_M \approx -\frac{1}{\sqrt{J}}, \tag{3.2}$$

for the value of ν for which $\mathcal{F}$ is maximum for $|\xi| > 1$. The corresponding angle φ_M is shown as a dotted line in Fig. 4b.

4. Application to localized PV distributions

a. Horizontally localized δ-PV

To gauge the significance of the directional effects discussed above on the structure of the GWs associated

with a 3D PV anomaly, we first consider the case of an infinitely thin PV distribution with Gaussian distribution in the horizontal direction:

$$q_0'(x,y,z) = \sigma_z q_r e^{-(x^2+y^2)/(2\sigma_H^2)}\delta(z), \tag{4.1}$$

where σ_H gives the characteristic horizontal width of the PV anomaly, q_r is its characteristic amplitude, and σ_z is its characteristic depth. The introduction of the scale σ_z naturally follows from the fact that $\delta(z)$ scales as an inverse length. For such a distribution, the vertical velocity field in (2.9) reads

$$w'(x,y,z) = \sigma_z \int_0^\infty \int_0^{2\pi} \hat{w}_0(K,\varphi) e^{i(kx+ly)} W\left(\varphi; \frac{k\Lambda z}{f}\right) K\, d\varphi\, dK = \sigma_z w_0'(x,y,z), \tag{4.2}$$

where for clarity we have made explicit the dependence of W on φ, and where

$$\hat{w}_0(K,\varphi) = -i\frac{\rho_r g(1+\tan^2\varphi)}{\theta_r \Lambda^2}\frac{q_r \sigma_H^2}{2\pi} e^{-(K^2\sigma_H^2)/2}, \tag{4.3}$$

according to the scaling in (2.12) and introducing the Fourier transform of (4.1). Note that w_0' is defined in (4.2) to simplify the notation in the full 3D case treated at the end of the section.

To evaluate the double integral in (4.2) we next proceed numerically by tabulating in the vertical direction the structure function $W(\varphi;\xi)$ for 180 discrete values of φ. This yields an angular resolution $\Delta\varphi = 2°$. We also consider 50 discrete values for the horizontal wavenumber K, with a resolution $\Delta K = \pi/(10\sigma_H)$. For the physical grid we take for both horizontal directions the resolution $\Delta x = \Delta y = 0.2\sigma_H$.

In the following, we express our results in dimensional form. We consider a $\sigma_z = 1$-km-thick layer of stratospheric air entering in the troposphere. We therefore take a PV amplitude of $\rho_r q_r = 1$ potential vorticity units (PVU; 1 PVU $\equiv 1 \times 10^{-6}$ K kg^{-1} m^2 s^{-1}) and assume $\sigma_H = 55$ km. Assuming that this air enters the troposphere at midlatitudes, we take $\rho_r = 1$ kg m^{-3}, $N = 0.01$ s^{-1}, $\theta_r = 300$ K, $f = 10^{-4}$ s^{-1}, and $J = 4$.

b. Vertical velocity field

The vertical velocity calculated from (4.2) is shown in Fig. 5 for six different altitudes. Near the PV anomaly [i.e., for $z = 0$ km (Fig. 5a)], the vertical velocity is positive to the east of the positive PV anomaly and negative to the west. This is of course consistent with the balanced picture that the meridional geostrophic winds are toward the north on the eastern flank of a positive PV anomaly, and to the south on the western flank (not shown). As the advective terms are very small in the thermodynamic equation (2.1d) at this altitude, the vertical velocity balances the meridional advection of the background potential temperature ($f\Lambda v' \approx N^2 w'$). At the higher altitude $z = 1$ km (Fig. 5b), the signal in vertical velocity decays in magnitude and spreads in horizontal scale, consistent with the QG predictions that all wavelengths decay exponentially with altitude, with the long wavelengths decaying less rapidly than the short ones. Note, however, the two large-scale lobes of opposite sign of the vertical velocity that have moved slightly to the north, which is a first sign that the QG prediction starts to break down (the QG prediction is insensitive to the sign of ν; see appendix B). At $z = 2$ km (Fig. 5c), the signal in vertical velocity has decayed further in magnitude and spread farther horizontally (note the contour interval decrease between Figs. 5b and 5c), again somehow in agreement with the QG prediction. Nevertheless, the two large-scale lobes of vertical velocity start to be modulated by a smaller-scale oscillatory signal, clearly apparent aloft the PV disturbance. Higher up in altitude this oscillatory signal entirely dominates the response; its lines of constant phase make a positive angle with the longitude axis because the waves with $\nu < 0$ are less absorbed at the inertial levels than those with $\nu > 0$. Note also that the amplitude between $z = 3$ and 10 km increases in agreement with the $z^{1/2}$ dependence predicted in (2.27). Because of the superposition of wavenumbers, the transition between decaying and wavelike perturbation does not occur sharply at a single inertial level but rather smoothly across an inertial-layer region. The altitude of the center of this region is given by the estimate $\sigma_H f/\Lambda \approx 1.1$ km, consistent with Fig. 5.

c. EP-flux vector

The EP flux in (2.29) is significant because its vertical derivative gives the x component of the force exerted by the GWs on the (transformed Eulerian) mean flow (Andrews et al. 1987). Because our model (2.1) is both x and y independent and the GWs are plane waves in both directions, the two horizontal components of the force can in fact be obtained from the EP-flux vector (or, up to a sign, vertical pseudomomentum-flux vector)

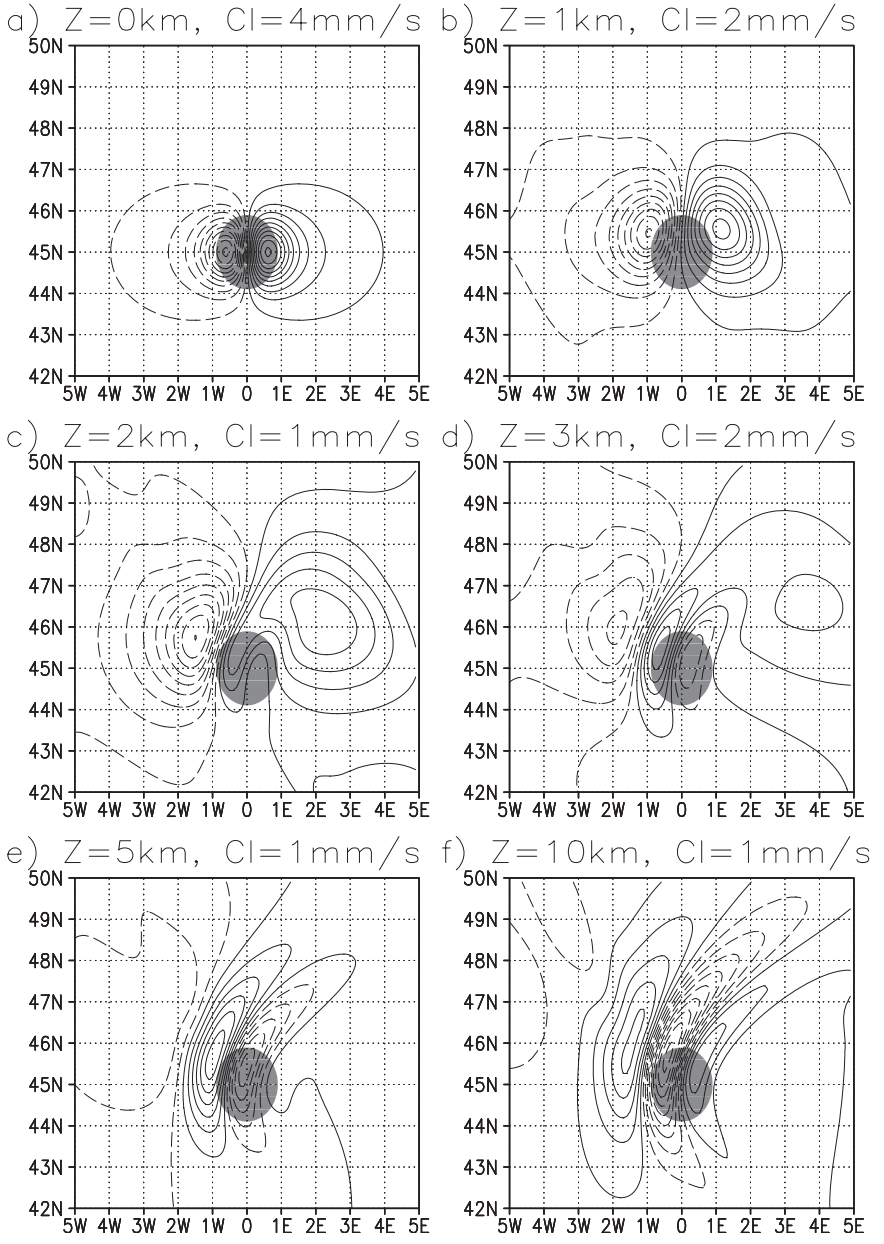

FIG. 5. Vertical velocity at various altitudes above a PV anomaly with a Gaussian distribution in the horizontal and Dirac distribution in the vertical. Solid (dashed) contours correspond to positive (negative) values. The gray shading indicates that the disturbance PV $\rho_r q_0'(x, y) > 0.2$ PVU.

$$-\left(\overline{u'w'} - f\frac{\overline{v'\theta'}}{\theta_{0z}}, \overline{v'w'} + f\frac{\overline{u'\theta'}}{\theta_{0z}}\right) \qquad (4.4)$$

[see Bühler (2009, section 8.2) and the discussion on the angular momentum flux in Jones (1967)]. The two components of this EP-flux vector are in proportion to k and l, since these are the proportion of the x and y components of the corresponding pseudomomentum density (Bühler 2009). The nondimensional EP-flux vector can therefore be written as $(1, l/k)\mathcal{F}$.

This can be made transparent using Bretherton's (1969) interpretation of the EP flux as the wave stress exerted by pressure force on undulating isentropes:

$$\mathbf{F} = \frac{1}{2\sigma_H^2}\int\int p'\nabla\eta'\,dx\,dy = \frac{2\pi^2}{\sigma_H^2}\int\int -i\mathbf{k}\hat{p}\hat{\eta}^*\,dk\,dl, \qquad (4.5)$$

where η' denotes the vertical displacement satisfying $D_t\eta' = w'$, and the factor $1/(2\sigma_H^2)$ is introduced in the definition of the average so that **F** has the dimension of a pressure. Using $ik\Lambda z\hat{\eta} = \hat{w}$ and the disturbance equations (2.1), we obtain

$$-i\mathbf{k}\hat{p}\hat{\eta}^* = -\rho_r\left(\hat{u}\hat{w}^* - f\frac{\hat{v}\hat{\theta}^*}{\theta_{0z}}, \hat{v}\hat{w}^* + f\frac{\hat{u}\hat{\theta}^*}{\theta_{0z}},\right) \quad (4.6)$$

in agreement with (4.4). Using the scaling in (2.10) and the structure function (2.11a), this relation leads to the EP-flux vector of a single plane wave,

$$-i\mathbf{k}\hat{p}\hat{\eta}^* = \frac{\mathbf{k}}{k}\frac{\rho_r\Lambda}{f}\frac{\sigma_z^2|\hat{w}_0|^2}{1+\nu^2}\left(i\frac{1-\xi^2}{\xi^2}W_\xi W^* - \nu\frac{WW^*}{\xi^2}\right)$$
$$= \frac{\rho_r\Lambda^4\sigma_z^2|\hat{w}_0|^2}{N^3 f(1+\nu^2)^2}\frac{\mathbf{k}}{K}\mathcal{F}, \quad (4.7)$$

where $\mathcal{F}$ is as in (2.28). For the localized PV distribution (4.3) the EP-flux vector then becomes

$$\mathbf{F} = F_0\int_0^\infty\int_0^{2\pi}\sigma_H^2\mathbf{k}e^{-K^2\sigma_H^2}\mathcal{F}\left(\varphi, \frac{k\Lambda z}{f}\right)d\varphi\, dK. \quad (4.8)$$

The scaling factor F_0 is given in (1.2) and is exactly the same as in LPV10. For the parameters chosen, it is about

$$F_0 = 10\,\text{Pa} \quad (4.9)$$

and directly gives the amplitude of the EP-flux vector since the double integral in (4.8) is nondimensional.

The exact results for the EP-flux vector in (4.8) are shown in Fig. 6 for two different values of J. When $J = 4$, **F** at $z = 0$ is purely zonal, with a magnitude near 5 mPa. The zonal orientation follows from the symmetry of the PV distribution about the x axis. At higher altitudes, **F** decreases in amplitude and changes direction. These two effects result from the absorption of an increasingly large portion of the wave spectrum at inertial levels, and from the fact that waves with $\nu < 0$ are much less absorbed than those with $\nu > 0$. When $J = 4$, **F** as $z \to \infty$ makes an angle close to $\varphi \approx -30°$ with the x axis, almost the angle for which the normalized EP flux has a maximum according to (3.2) (see also Fig. 4b). For $J = 10$ (Fig. 6b), **F** in the far field has an amplitude that is about half that at $z = 0$, and it makes an angle with the x axis that is close to $\varphi \approx -15°$, a value again consistent with (3.2).

For practical purposes it is useful to estimate the EP-flux vector near the PV anomaly and in the far field using the WKB form for $\mathcal{F}$ in (2.31). Introducing (2.31), (4.8) becomes

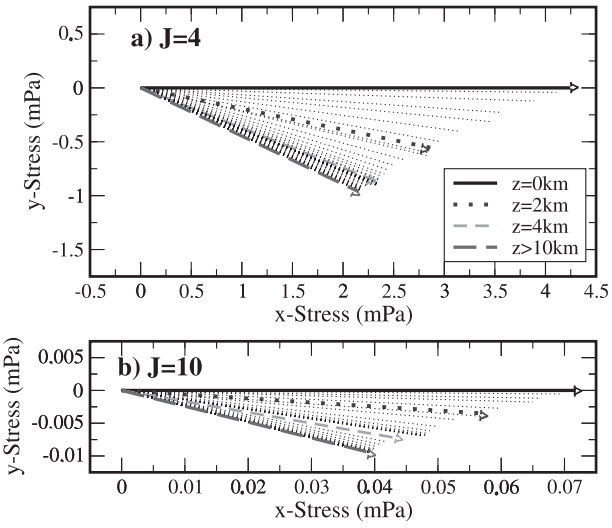

FIG. 6. EP-flux vector as a function of altitude for the PV distribution used in Fig. 5 for (a) $J = 4$ and (b) $J = 10$. The dashed lines represent the vector every 200 m typically; the thick vectors correspond to the altitudes indicated in (a).

$$\mathbf{F}(0^+) \approx \frac{F_0}{4}\int_{-\pi/2}^{\pi/2}\cos\varphi\hat{\mathbf{x}}e^{-\pi\sqrt{J(1+\nu^2)}-\nu\pi}d\varphi, \quad (4.10a)$$

$$\mathbf{F}(\infty) \approx \frac{F_0}{8}\int_{-\pi/2}^{\pi/2}(\cos\varphi\hat{\mathbf{x}} + \sin\varphi\hat{\mathbf{y}})e^{-\pi\sqrt{J(1+\nu^2)}-\nu\pi}d\varphi, \quad (4.10b)$$

where $\hat{\mathbf{x}}$ and $\hat{\mathbf{y}}$ are the zonal and meridional unit vectors. Since the WKB approximation assumes $J \gg 1$ is large, these expressions can be further simplified using Laplace's method to obtain

$$\mathbf{F}(0^+) \approx \frac{F_0}{2\sqrt{2\sqrt{J}}}e^{-\pi\sqrt{J}}\hat{\mathbf{x}},$$
$$\mathbf{F}(\infty) \approx \frac{F_0}{4\sqrt{2\sqrt{J}}}e^{-\pi\sqrt{J}}(\hat{\mathbf{x}} - J^{-1/2}\hat{\mathbf{y}}). \quad (4.11)$$

These formulas give very good approximations for the EP-flux vector for $z \ll 1$ and $z \gg 1$ when $J \gg 1$ as in Fig. 6b, but they underestimate it by a factor of almost 2 when $J \approx 1$.

Comparing (4.11) to the 2D results in LPV10 [see also (1.1) and (1.2)] shows that the orders of magnitude of **F** are comparable in 2D and 3D (the F_0 term), and that in both cases about half of the EP flux in the direction of the shear is deposited in the inertial layer. The most remarkable difference is that the EP-flux vector rotates with altitude. Consider, for example, a westerly shear in the Northern Hemisphere: the EP-flux vector tends, for large z, to an angle close to $\varphi_M = -1/\sqrt{J}$ to the right of the shear. As a consequence, the disturbance produced

by the PV anomaly exerts a southwestward drag on the large-scale flow in the upper inertial layer and, assuming dissipation at high altitude, a northwestward drag in the far field aloft. Both drags are almost equal in the direction of the shear (as in the 2D case) and opposite in the transverse direction. More generally, the transverse component of the drag in the inertial layers is to the right of the wind (e.g., northward at the lower inertial layer in the above example), and to the left in the Southern Hemisphere.

d. Horizontally localized, finite depth PV

The PV distributions used so far were infinitely thin and thus neglected the effect of the vertical shear on the PV distribution itself and consequent time evolution of the wave field. As this aspect has been detailed in the 2D case by LPV10, we only describe it briefly here. As in LPV10, we consider a PV distribution at $t = 0$ that is separable in the horizontal and the vertical directions and that has the same vertical integral as (4.1):

$$q_0'(x,y,z) = q_r e^{-(x^2+y^2)/2\sigma_H^2} \begin{cases} \cos^2[\pi z/(2\sigma_z)] & \text{for} \quad |z| < \sigma_z \\ 0 & \text{for} \quad |z| > \sigma_z \end{cases}. \tag{4.12}$$

To compute the vertical integral in the response at a low numerical cost, we take full advantage of the preceding calculations and discretize q_0' as

$$q_0' \approx q_r e^{-(x^2+y^2)/2\sigma_H^2} \sum_{-M+1}^{M-1} \cos^2[\pi z_m/(2\sigma_z)]\Delta z \delta(z - z_m), \tag{4.13}$$

where $z_m = m\Delta z$ and $\Delta z = \sigma_z/M$. In this case, the vertically discretized equivalent of the vertical velocity in (2.9) reduces to

$$w'(x,y,z,t) \approx \sum_{-M+1}^{M-1} \cos^2\left(\frac{\pi z_m}{2\sigma_z}\Delta z\right) w_0'(x - \Lambda z_m t, y, z - z_m), \tag{4.14}$$

where w_0' is the function introduced in (4.2). Because x and t enter (4.14) only in the combination $x - \Lambda z_m t$, the computation of the sum over the indices m involves straightforward vertical and horizontal translations of w_0'.

Figure 7 shows the evolution of the integral of the disturbance PV, $\int_{-\infty}^{+\infty} q'(x,y,z,t)\,dz$, and of the vertical velocity at the altitude $z = 10$ km, for $\sigma_z = 1$ km and $J = 4$. All of the other parameters are as in the previous sections. The solution is only shown for negative values of t: for positive t it is almost symmetric to that at negative t. The background velocity shears the PV whose horizontal extent therefore decreases with time until $t = 0$ before increasing again. When it is more spread out horizontally (that is at large negative or positive time), its vertical integral is also relatively small compared to its value at $t = 0$. As a result, the vertical velocity increases as t increases toward 0.

Comparing the four panels in Fig. 7 to the time-independent disturbance produced by the δ-PV of Fig. 5 indicates that the amplitude of the GW patterns are comparable at $t = 0$ and ± 6 h but substantially smaller at $t = \pm 12$ and ± 18 h. Accordingly, it is only in time intervals of half a day or so that the values for GWs emission and for the associated EP flux given in the previous sections apply.

5. Conclusions

The linear motion associated with 3D localized potential vorticity (PV) anomalies in the presence of an unbounded vertical shear Λ has been analyzed in the linear approximation. Exact and approximate solutions were obtained analytically for PV anomalies that are monochromatic in x and y, and vary as a Dirac delta function $\delta(z)$ in the vertical. Combinations of these yield solutions for more general PV anomalies.

A PV anomaly of horizontal scale σ_H at $z = 0$ induces two inertial critical layers at $z = \pm\sigma_H f/\Lambda$. Through these levels, the intrinsic frequency of the disturbance increases from subinertial to superinertial. Correspondingly, there is a transition from balanced near $z = 0$ (where the solutions can be described as quasigeostrophic) to sheared GW for $|z| > \sigma_H f/\lambda$. The amplitude of the GW is approximately

$$\exp\left[-\sqrt{J(1+\nu^2)}\pi/2 - \nu\pi\right]/J/(1+\nu^2),$$

where $J = N^2/\Lambda^2$ is the Richardson number and $\nu = l/k$ is the ratio of the y and x components of the wave vector. As previously noted (LPV10), these waves can be substantial for moderate Richardson numbers, say J between 1 and 10. The present analysis reveals a new, remarkable result: the emitted waves have a strong meridional asymmetry, with larger amplitudes for waves with $\nu < 0$. For example, in a westerly shear in the Northern Hemisphere, waves aloft having their wave vector pointing to the southeast will be larger than waves with their wave vector pointing to the northeast (see Figs. 5 and 7). Using the exact analytical solutions we show how this asymmetry, in a symmetric background flow, is related to the meridional slope of the

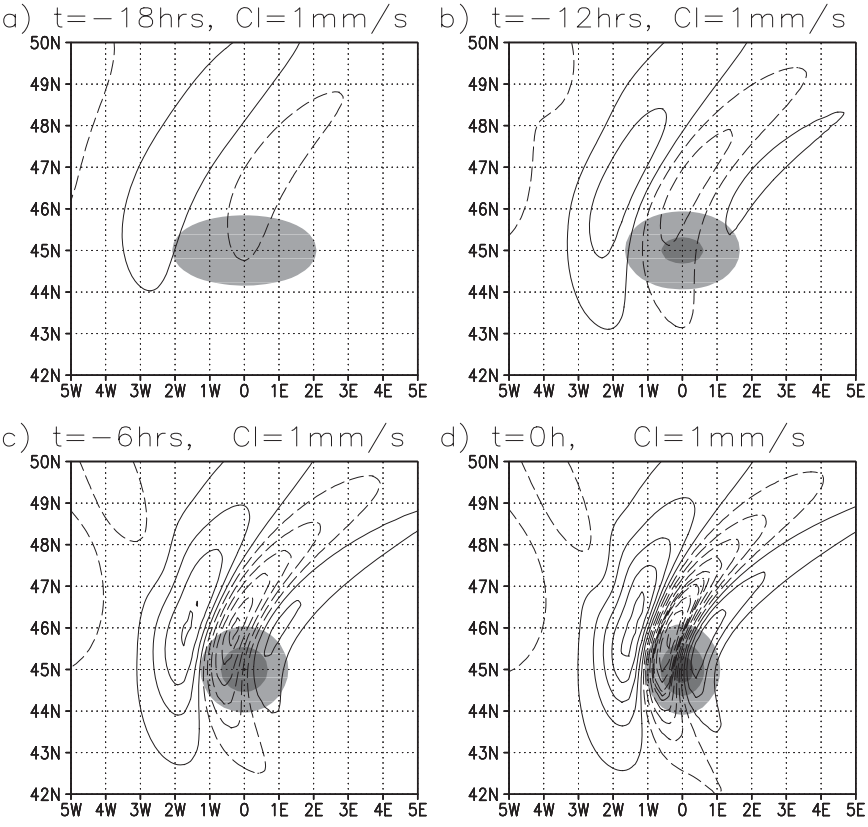

FIG. 7. Vertical velocity at $z = 10$ km above a PV anomaly with a Gaussian distribution in the horizontal and a finite depth in the vertical. Solid (dashed) contours correspond to positive (negative) values. The three shades of gray indicate vertical integrals of the PV disturbance greater than 0.1, 0.45, and 0.9 PVU km.

isentropes (see Fig. 2). This asymmetry has been identified previously in studies of gravity waves propagating toward critical levels in a constant shear (the valve effect) (Yamanaka and Tanaka 1984).

One implication is a strong sensitivity to orientation (i.e., to ν) of the absorption of the Eliassen–Palm flux through the inertial levels: there is almost no jump when ν is large and negative, in contrast to nearly complete absorption when ν is large and positive [see (2.31) and (2.32) and Fig. 4]. Hence the drag due to the waves absorbed within the upper inertial layer has a substantial component oriented to the right of the shear in the Northern Hemisphere (southeast in the above example). The WKB solutions provide simple expressions for the fluxes, the angle maximizing them, and the drag, in very good agreement with the exact analytical solutions (see Fig. 4).

The relevance of this emission in real flows remains to be assessed. Nonetheless, two points are worth noting: first, it has been noted from satellite observations (Wu and Eckermann 2008) and from high-resolution numerical weather prediction (NWP) models (Shutts and Vosper 2011) that gravity waves in the midlatitudes have a favored orientation: phase lines with a northeast-to-southwest tilt in the Northern Hemisphere, and with a northwest-to-southeast tilt in the Southern Hemisphere. Waves with these orientations are conspicuous in the stratospheric polar night jets of both hemispheres (i.e., in regions with strong positive vertical shear). The reasons for this favored orientation are not clear.[1] It is noteworthy that this orientation is consistent with that expected in the case of emission from sheared PV anomalies. Whether this emission is occurring or this is only a coincidence due to a more fundamental property of GW in shear remains to be investigated. Second, at smaller scales, we can expect this mechanism to play a role where the breaking of intense orographic gravity waves produces small-scale PV anomalies (Plougonven et al. 2010).

As discussed in LPV10, our results could be used for parameterizations in GCMs of GW emission by fronts at the tropopause (Charron and Manzini 2002; Richter

[1] Shutts and Vosper (2011) suggested that this tilt could be tied to the orientation of surface cold fronts, but gravity waves generated in idealized baroclinic life cycles (O'Sullivan and Dunkerton 1995; Plougonven and Snyder 2007) show the opposite tilt.

et al. 2010), where substantial intrusion of stratospheric air occurs and where strong shears are common. In this context the predictor given in LPV10 seems adapted, providing we add the transverse component of the EP flux as in (4.11). The factor 1/4 for the flux emitted by 2D PV disturbance in (1.1) should more accurately be $1/(2\sqrt{2\sqrt{J}})$ [see (4.11)], but they should probably be replaced by a tuning factor of order 1. In all cases the along-shear component of the EP-flux vector should decrease by a factor of 2 at the inertial levels and the transverse component in the far field should be oriented to the right of the shear with magnitude $1/\sqrt{J}$ times the along-shear component.

The present paper has shown that the formula given in LPV10 and recalled here in (1.1) and (1.2) applies quite well in the 3D case. To take directional effects into account one should use (4.11) rather than (1.1), keeping unchanged the dimensional factor (1.2).

Acknowledgments. FL was supported by the EU-FP7 project EMBRACE (Grant Agreement 282672), and RP and JV by the Alliance Programme of the French Foreign Affairs Ministry and British Council. JV also acknowledges the support of a NERC grant. We also thank Oliver Bühler for pointing out a useful reference.

APPENDIX A

Exact Solution for $W(\xi)$

To find a solution to (2.13), we first derive its homogeneous solutions for $\xi > 0$ and impose a radiation condition for $\xi \gg 1$ to obtain a solution that represents an upward-propagating GW. We deduce from this a solution valid for $\xi < 1$ that represents a downward-propagating GW for $\xi \ll -1$. The amplitudes of these two solutions are then chosen to satisfy the jump conditions

$$[W]_{0^-}^{0^+} = 0 \quad \text{and} \quad \left[\frac{W_\xi}{\xi^2}\right]_{0^-}^{0^+} = 1. \tag{A.1}$$

a. Homogeneous solution for $\xi > 0$

The changes of variables $W = (1 + \xi)^{-i\nu}$ and $\eta = \xi^2$ transform (2.13) into the canonical form of the hypergeometric equation [(15.5.1) in Abramowitz and Stegun (1964), hereafter AS]:

$$\eta(1 - \eta)Y_{\eta\eta} + [c - (a + b + 1)\eta]Y_\eta - abY = 0, \tag{A.2a}$$

$$\text{where} \quad a = -\frac{1}{4} - \frac{i}{2}\nu + \frac{i}{2}\mu, \quad b = -\frac{1}{4} - \frac{i}{2}\nu - \frac{i}{2}\mu,$$
$$c = -\frac{1}{2}, \quad \text{and} \tag{A.2b}$$

$$\mu = \sqrt{J(1 + \nu^2) - 1/4}. \tag{A.2c}$$

For $\xi > 1$ the two solutions of the hypergeometric equation (A.2a) are given by (15.5.7) and (15.5.8) in AS. We retain the second solution

$$W^{(u)}(\xi) = (1 + \xi)^{-i\nu}\xi^{-2b}F(a', b'; c'; \xi^{-2}), \tag{A.3}$$

where F is the hypergeometric function and $a = a'$, $b' = b' - c + 1$, $c' = b - a + 1$, because its asymptotic form,

$$W^{(u)}(\xi) \sim \xi^{1/2+i\mu} \quad \text{as} \quad \xi \to \infty, \tag{A.4}$$

corresponds to an upward propagating GW (Booker and Bretherton 1967).

For $0 < \xi < 1$ the solution to (A.2a) is best written as a linear combination of the two independent solutions (15.5.3) and (15.5.4) in AS:

$$W^{(u)}(\xi) = (1 + \xi)^{-i\nu}[AF(a, b; c; \xi^2) + B\xi^3F(a'', b''; c''; \xi^2)], \tag{A.5}$$

where $a'' = a - c + 1$, $b'' = b - c + 1$, $c'' = 2 - c$, and A and B are two complex constants.

To connect (A.5) to (A.3), we use the transformation formula for F [(15.3.6) in AS] and obtain the asymptotic approximations

$$W^{(u)}(\xi) \sim \alpha'(\xi - 1)^{i\nu} + \beta' \quad \text{as} \quad \xi \to 1^+, \tag{A.6a}$$

$$W^{(u)}(\xi) \sim (\alpha A + \alpha'' B)(1 - \xi)^{i\nu} + \beta A + \beta'' B \quad \text{as} \quad \xi \to 1^-. \tag{A.6b}$$

In these expressions,

$$\alpha = 2^{i\nu}\frac{\Gamma(c)\Gamma(a + b - c)}{\Gamma(a)\Gamma(b)} \quad \text{and} \quad \beta = \frac{\Gamma(c)\Gamma(c - a - b)}{\Gamma(c - a)\Gamma(c - b)}, \tag{A.7}$$

where Γ is the gamma function (AS, chapter 6). The other coefficients (α', β') and (α'', β'') are defined by the same formulas with (a, b) replaced by (a', b') and (a'', b''), respectively.

To continue the solution (A.6a) below the inertial level at $\xi = 1$, we follow Booker and Bretherton (1967) and introduce an infinitely small linear damping that shifts the real ξ axis into the lower half of the complex plane so that

$$\xi - 1 = (1 - \xi)e^{-i\pi} \quad \text{for} \quad \xi < 1. \tag{A.8}$$

Thus, (A.6a) matches (A.6b) provided that

$$\alpha A + \alpha'' B = \alpha' e^{\nu\pi} \quad \text{and} \quad \beta A + \beta'' B = \beta'. \quad \text{(A.9)}$$

This determines A and B and completes the evaluation of $W^{(u)}(\xi)$.

b. Solution over the entire domain

The solution for $\xi < 0$ can be deduced from $W^{(u)}(\xi)$ by noting that (2.13) applies to W^* when ξ is changed in $-\xi$. A possible solution is simply

$$W^{(d)}(\xi) = W^{(u)}(-\xi)^*. \quad \text{(A.10)}$$

This satisfies the radiation condition for $\xi \to -\infty$ since

$$W^{(d)}(\xi) \sim |\xi|^{1/2 - i\mu}, \quad \text{(A.11)}$$

which represents a downward-propagating GW.

The two solutions $W^{(u)}$ and $W^{(d)}$ can be combined to obtain a solution valid over the entire domain that satisfies the jump condition (A.1). This is given by

$$W(\xi) = \begin{cases} EW^{(u)}(\xi) & \text{for} \quad \xi > 0 \\ E^* W^{(d)}(\xi) & \text{for} \quad \xi < 0 \end{cases}, \quad \text{(A.12)}$$

where the constant E is found by imposing the jump condition (A.1) and given by

$$E = \frac{A^*}{3(AB^* + A^*B)}. \quad \text{(A.13)}$$

To verify this, we note that when $|\xi| \ll 1$, the upper and lower solutions in (A.12) have the asymptotic expansions

$$EA\left[1 - i\nu\xi - \left(\frac{\mu^2}{2} + \frac{1}{8}\right)\xi^2 - i\nu\left(\frac{\nu^2}{3} - \frac{\mu^2}{2} + \frac{5}{24}\right)\xi^3\right] + EB\xi^3, \quad \text{(A.14a)}$$

$$E^*A^*\left[1 - i\nu\xi - \left(\frac{\mu^2}{2} + \frac{1}{8}\right)\xi^2 - i\nu\left(\frac{\nu^2}{3} - \frac{\mu^2}{2} + \frac{5}{24}\right)\xi^3\right] - E^*B^*\xi^3 \quad \text{(A.14b)}$$

for $\xi > 0$ and $\xi < 0$, respectively. For the value of E in (A.13), EA is real, which implies that the first terms on the left-hand sides of (A.14a) and (A.14b) are identical, ensuring that $[W]_{0^-}^{0^+} = 0$ and they do not contribute to the jump $[W_\xi/\xi^2]_{0^-}^{0^+} = 1$ in (A.1); the second terms combine so that W_ξ/ξ^2 jumps by 1 at $\xi = 0$ as required. Note also that near $|\xi| = 0$, $W(\xi)$ approaches the value

$$W(0) = \frac{A^*A}{3(AB^* + A^*B)}. \quad \text{(A.15)}$$

APPENDIX B

WKB Approximation

In this appendix, we derive the WKB approximations (2.16)–(2.19) for W in regions (i)–(iv) and provide details of the matching procedure.

For region (i), we introduce $\zeta = \sqrt{J(1+\nu^2)}\xi = O(1)$ into (2.13) to obtain at leading order the geostrophic approximation

$$\frac{W_{\zeta\zeta}}{\zeta^2} - 2\frac{W_\zeta}{\zeta^3} - \frac{W}{\zeta^2} = \frac{\delta(\zeta)}{[J(1+\nu^2)]^{3/2}}. \quad \text{(B.1)}$$

The solution is readily found and given in terms of $\xi > 0$ by (2.16).

For regions (ii) and (iv), the standard WKB expansion

$$W(\xi) = (W_0 + J^{-1/2}W_1 + \cdots)e^{\sqrt{J(1+\nu^2)}\int^\xi \phi(\xi')d\xi'} \quad \text{(B.2)}$$

gives at $O(J)$ and $O(J^{1/2})$

$$\phi = \frac{\pm 1}{\sqrt{1-\xi^2}} \quad \text{and} \quad W_0 = \frac{\xi}{(\xi-1)^{1/4 - i\nu/2}(\xi+1)^{1/4 - i\nu/2}}, \quad \text{(B.3)}$$

respectively. The forms (2.17) and (2.19) of the solution follow immediately.

For region (iii), finally, we introduce the variable $\zeta = J(1+\nu^2)(\xi - 1) = O(1)$. To leading order (2.13) then reduces to

$$2\zeta W_{\zeta\zeta} + 2(1 - i\nu)W_\zeta + W = 0, \quad \text{(B.4)}$$

whose solution is given in terms of Hankel functions in (2.19). The following asymptotic equations [(9.2.3) and (9.2.4) in AS] are needed to match this solution to the solutions in regions (ii) and (iv):

$$H_{i\nu}^{(1)}(x) \sim \sqrt{\frac{2}{\pi x}} e^{\nu\pi/2} e^{i(x - \pi/4)} \quad \text{as} \quad |x| \to \infty \quad \text{for} \quad -\pi < \arg x < 2\pi, \quad \text{and} \quad \text{(B.5)}$$

$$H_{i\nu}^{(2)}(x) \sim \sqrt{\frac{2}{\pi x}} e^{-\nu\pi/2} e^{-i(x - \pi/4)} \quad \text{as} \quad |x| \to \infty \quad \text{for} \quad -2\pi < \arg x < \pi. \quad \text{(B.6)}$$

Using these, we find from (2.18) that

$$W \sim \frac{2^{1/4}}{\sqrt{\pi}\zeta^{1/4-i\nu/2}}[A^{(\mathrm{iii})}e^{\nu\pi/2}e^{i(\sqrt{2\zeta}-\pi/4)} + B^{(\mathrm{iii})}e^{-\nu\pi/2}e^{-i(\sqrt{2\zeta}-\pi/4)}] \quad \text{(B.7)}$$

as $\xi \to \infty$. Matching with the limiting behavior of (2.16) as $\xi \to 1$ gives (2.21).

To match the solutions between regions (ii) and (iii), we need to consider the limit of the Hankel functions for $\zeta = |\zeta|e^{-i\pi}$ with $|\zeta| \to \infty$, in accordance with the analytic continuation (A.5). Proceeding in similar fashion as above using (B.5) yields relation (2.22) between $A^{(\mathrm{ii})}$ and $A^{(\mathrm{iii})}$, but $B^{(\mathrm{iii})} = 0$. As mentioned, $B^{(\mathrm{ii})} = 0$ is inconsistent with the nonzero EP flux expected because of the wave radiation as $|\zeta| \to \infty$. To resolve this difficulty, we need to employ a more sophisticated matching that recognizes that $B^{(\mathrm{ii})}$ takes in fact a nonzero exponentially small value and provides an estimate for this value.

The nonzero value of $B^{(\mathrm{ii})}$ arises as a result of a Stokes phenomenon (e.g., Ablowitz and Fokas 1997): the line $\zeta < 0$ ($\arg\zeta = -\pi$) is a Stokes line, where one solution (here multiplied by $A^{(\mathrm{ii})}$) is maximally dominant over the other, recessive solution (multiplied by $B^{(\mathrm{ii})}$). Across this Stokes line, the dominant solution switches on the recessive solution with an amplitude given by an exponentially small Stokes multiplier. Thus, below the Stokes line the amplitude $B^{(\mathrm{ii})} = 0$, and above it $B^{(\mathrm{ii})} \neq 0$ is given by the Stokes multiplier; on the Stokes line itself, $B^{(\mathrm{ii})}$ is half the Stokes multiplier (Berry 1989). To obtain the Stokes multiplier, we need a large $|\zeta|$ formula for (2.18) that is valid for $-3\pi < \arg\xi < -\pi$ so that it holds immediately above the Stokes line and also on the anti-Stokes line $\arg\zeta = -2\pi$ where the two solutions have the same order and hence can be identified unambiguously. Such a formula is obtained using the connection equation [(9.1.37) in AS] to obtain

$$H_{i\nu}^{(1)}(\sqrt{2\zeta}) = 2\cosh(\nu\pi)H_{i\nu}^{(1)}(e^{i\pi}\sqrt{2\zeta}) + e^{\nu\pi}H_{i\nu}^{(2)}(e^{i\pi}\sqrt{2\zeta}). \quad \text{(B.8)}$$

For $-3\pi < \arg\zeta < -\pi$, $-\pi/2 < \arg(e^{i\pi}\sqrt{2\zeta}) < \pi/2$, and (B.5) and (B.6) can be applied to obtain the large-$|\zeta|$ asymptotics

$$H_{i\nu}^{(1)}(\sqrt{2\zeta}) \sim \frac{2^{1/4}}{\sqrt{\pi}\zeta^{1/4}}e^{\nu\pi/2}[2\cosh(\nu\pi)e^{-3i\pi/4}e^{-i\sqrt{2\zeta}} + e^{-i\pi/4}e^{i\sqrt{2\zeta}}]. \quad \text{(B.9)}$$

Introducing this into (2.18) with $B^{(\mathrm{iii})} = 0$ and using that $\xi = J(1+\nu^2)(1-\xi)e^{-i\pi}$ leads to

$$W \sim \frac{2^{1/4}e^{\nu\pi}[J(1+\nu^2)]^{-1/4+i\nu/2}}{\sqrt{\pi}(1-\xi)^{1/4-i\nu/2}}A^{(\mathrm{iii})}[e^{\sqrt{J(1+\nu^2)}\sqrt{2(1-\xi)}} - 2i\cosh(\nu\pi)e^{-\sqrt{J(1+\nu^2)}\sqrt{2(1-\xi)}}]. \quad \text{(B.10)}$$

Matching with the limit of (2.17) as $\xi \to 1$ gives (2.22), and (2.23) on taking into account that Stokes multiplier on the Stokes line is half its value away from it.

The matching between regions (i) and (ii) yielding (2.25) and (2.26) is straightforward.

REFERENCES

Ablowitz, M. J., and A. S. Fokas, 1997: *Complex Variables: Introduction and Applications*. Cambridge University Press, 647 pp.

Abramowitz, M., and I. A. Stegun, 1964: *Handbook of Mathematical Functions*. 9th ed. Dover, 1045 pp.

Andrews, D. G., J. R. Holton, and C. B. Leovy, 1987: *Middle Atmospheric Dynamics*. Academic Press, 489 pp.

Bender, C. M., and S. A. Orszag, 1999: *Advanced Mathematical Methods for Scientists and Engineers*. Springer, 593 pp.

Berry, M. V., 1989: Uniform asymptotic smoothing of Stokes's discontinuities. *Proc. Roy. Soc. London,* **422A,** 7–21.

Booker, J. R., and F. P. Bretherton, 1967: The critical layer for internal gravity waves in a shear flow. *J. Fluid Mech.,* **27,** 513–539.

Bretherton, F. P., 1969: Momentum transport by gravity waves. *Quart. J. Roy. Meteor. Soc.,* **95,** 213–243.

Bühler, O., 2009: *Waves and Mean Flows*. Cambridge University Press, 341 pp.

Charron, M., and E. Manzini, 2002: Gravity waves from fronts: Parameterization and middle atmosphere response in a general circulation model. *J. Atmos. Sci.,* **59,** 923–941.

Eliassen, A., and E. Palm, 1961: On the transfer of energy in stationary mountain waves. *Geophys. Publ.,* **22,** 1–23.

Ford, R., M. E. McIntyre, and W. A. Norton, 2000: Balance and the slow quasimanifold: Some explicit results. *J. Atmos. Sci.,* **57,** 1236–1254.

Grimshaw, R., 1975: Internal gravity waves: Critical level absorption in a rotating fluid. *J. Fluid Mech.,* **70,** 287–304.

Hertzog, A., G. Boccara, R. A. Vincent, F. Vial, and P. Cocquerez, 2008: Estimation of gravity wave momentum flux and phase speeds from quasi-Lagrangian stratospheric balloon flights. Part II: Results from the Vorcore campaign in Antarctica. *J. Atmos. Sci.,* **65,** 3056–3070.

Inverarity, G. W., and G. J. Shutts, 2000: A general, linearized vertical structure equation for the vertical velocity: Properties, scalings and special cases. *Quart. J. Roy. Meteor. Soc.,* **126,** 2709–2724.

Jones, W. L., 1967: Propagation of internal gravity waves in fluids with shear flow and rotation. *J. Fluid Mech.,* **30,** 439–448.

Lott, F., 2003: Large-scale flow response to short gravity waves breaking in a rotating shear flow. *J. Atmos. Sci.,* **60,** 1691–1704.

——, R. Plougonven, and J. Vanneste, 2010: Gravity waves generated by sheared potential vorticity anomalies. *J. Atmos. Sci.,* **67,** 157–170.

Mamatsashvili, G. R., V. R. Avsarkisov, G. D. Chagelishvili, R. G. Chanishvili, and M. V. Kalashnik, 2010: Transient dynamics of nonsymmetric perturbations versus symmetric instability in baroclinic zonal shear flows. *J. Atmos. Sci.,* **67,** 2972–2989.

Martin, A., 2008: Influence des ondes de gravité de montagne sur l'écoulement de grande échelle en présence de niveaux critiques. Ph.D thesis, Université Pierre et Marie Curie, 178 pp.

O'Sullivan, D., and T. J. Dunkerton, 1995: Generation of inertia–gravity waves in a simulated life cycle of baroclinic instability. *J. Atmos. Sci.,* **52,** 3695–3716.

Pedlosky, J., 1987: *Geophysical Fluid Dynamics*. 2nd ed. Springer-Verlag, 710 pp.

Plougonven, R., and C. Snyder, 2007: Inertia–gravity waves spontaneously generated by jets and fronts. Part I: Different baroclinic life cycles. *J. Atmos. Sci.,* **64,** 2502–2520.

——, D. J. Muraki, and C. Snyder, 2005: A baroclinic instability that couples balanced motions and gravity waves. *J. Atmos. Sci.,* **62,** 1545–1559.

——, A. Arsac, A. Hertzog, L. Guez and F. Vial, 2010: Sensitivity study for mesoscale simulations of gravity waves above Antarctica during Vorcore. *Quart. J. Roy. Meteor. Soc.,* **136,** 1371–1377.

Richter, J. H., F. Sassi, and R. R. Garcia, 2010: Toward a physically based gravity wave source parameterization in a general circulation model. *J. Atmos. Sci.,* **67,** 136–156.

Rossby, C. G., 1937: On the mutual adjustment of pressure and velocity distributions in certain simple current systems. *J. Mar. Res.,* **1,** 15–28.

Scavuzzo, C. M., M. A. Lamfri, H. Teitelbaum, and F. Lott, 1998: A study of the low-frequency inertio-gravity waves observed during the Pyrénées Experiment. *J. Geophys. Res.,* **103** (D2), 1747–1758.

Schär, C., and R. B. Smith, 1993: Shallow-water flow past isolated topography. Part I: Vorticity production and wake formation. *J. Atmos. Sci.,* **50,** 1373–1400.

Shepard, H. K., 1983: Decay widths for metastable states: Improved WKB approximation. *Phys. Rev.,* **27D,** 1288–1298.

Shutts, G. J., and S. B. Vosper, 2011: Stratospheric gravity waves revealed in NWP model forecasts. *Quart. J. Roy. Meteor. Soc.,* **137,** 303–317.

Vanneste, J., 2008: Exponential smallness of inertia–gravity wave generation at small Rossby number. *J. Atmos. Sci.,* **65,** 1622–1637.

——, and I. Yavneh, 2004: Exponentially small inertia–gravity waves and the breakdown of quasigeostrophic balance. *J. Atmos. Sci.,* **61,** 211–223.

Wu, D. L., and S. D. Eckermann, 2008: Global gravity wave variances from *Aura* MLS: characteristics and interpretation. *J. Atmos. Sci.,* **65,** 3695–3718.

Yamanaka, M. D., 1985: Inertial oscillation and symmetric motion induced in an inertio-gravity wave critical layer. *J. Meteor. Soc. Japan,* **63,** 715–736.

——, and H. Tanaka, 1984: Propagation and breakdown of internal inertio-gravity waves near critical levels in the middle atmosphere. *J. Meteor. Soc. Japan,* **62,** 1–16.